Spin-Injection Enhancements in van der Waals Magnetic Tunnel Junctions through Barrier Engineering

Jonathan J. Heath and Marcelo A. Kuroda [*]

Department of Physics, Auburn University, Auburn, Alabama 36849, USA

The weak interlayer coupling in two-dimensional materials enables the formation of sharp crystalline magnetic tunnel junctions without the epitaxial constraints found in the bulk. Amid the large number of heterostructures that can be formed using these layered materials, a means to guide the experimental design of systems with enhanced responses is desired. Here, we attain meaningful improvements in spin injection by tailoring the tunneling barriers through the choice of the metal electrodes. Owing to the weak coupling, the barrier engineering can be rationalized from properties of bulk components from first-principles calculations, leading to superior spin injection and magnetoresistance. Analysis of CrI_3 junctions formed with transition-metal dichalcogenide electrodes shows that junction conductivities increase by nearly 3 orders of magnitude with respect to those experimentally demonstrated with graphite leads. Moreover, we find that tunneling magnetoresistance significantly augments with low-work-function electrodes when carriers are injected near the CrI_3 conduction-band edge. The predictive approach employed in this work shows good agreement with detailed quantum transport calculations and can potentially accelerate the design of tunnel junctions based on two-dimensional materials.

Heterostructures formed with two-dimensional (2D) materials are receiving considerable attention as platforms for a variety of innovative physical phenomena, which benefit from sharp interfaces, few-atom thicknesses, and the weak van der Waals (vdW) coupling [1,2]. Recent experimental demonstrations of magnetic tunnel junctions (MTJs) based on few-layer CrX_3 (X = Cl, Br, or I) have reported tunneling magnetoresistance (TMR) values in the range of 50%–200% for bilayer junctions [3,4], which can be substantially enlarged in multilayer CrI_3 channels through electrostatic gating [5–8]. Despite the colossal TMR achieved in these devices, the use of graphitic leads in concert with the CrX_3 channel yields low conductivity values ($\lesssim 10^{-7}$ S μm^{-2} in bilayer junctions [3,4]) due to the vanishing density of states (DOS) of graphene near the Fermi level. In addition to facilitating readout, high current densities (in and out of plane) may be exploited as switching mechanisms via spin-orbit torque [9,10]. Therefore, identifying alternative electrode materials is imperative to meaningfully advancing the development of these junctions.

The investigation of 2D-material spintronic devices has spawned a variety of efforts [11]. For instance, theoretical studies have proposed the use of Cu leads in CrI_3 junctions [12] or magnetic transition-metal dichalcogenides (TMDs) such as magnetic $1T$-VX_2 (X = Se or Te) as lead or channel materials [13–15] as mechanisms to enhance the TMR response. Complementarily, experimental endeavors have also explored changes in the channel or electrodes to form improved junctions based on 2D materials [16–21]. However, the continuously growing family of 2D materials and the absence of epitaxial constraints between layers give innumerable material combinations, demanding guiding principles for the optimal design of these vdW heterostructures.

Here, we exploit barrier engineering to form 2D-material heterostructures with increased conductivities and TMR. The design guidelines are based on the physical properties of individual constituents (electrodes and channels) obtained from first principles. In exemplary systems with CrI_3 tunneling barriers and TMD electrodes, we find that TMD electrodes yield conductivities nearly 3 orders of magnitude larger than those attained with graphite electrodes. More importantly, we anticipate meaningful improvements in TMR using low-work-function electrodes in CrI_3 (and $CrBr_3$) junctions. We compare the predictions of this approach to more detailed descriptions of tunneling using the nonequilibrium Green's function (NEGF) formalism. We discuss the virtues and limitations of this design scheme that, by prioritizing material candidates using bulk or isolated properties, may foster rapid advancements in 2D-material-based tunnel junctions.

[*]mkuroda@auburn.edu

Improvements of MTJ characteristics must ensure an increase in either tunneling current or TMR, ideally both. Two physical parameters of vdW heterostructures are *a priori* key to enhance these quantities: (i) energy-dependent tunneling rates of the channel associated with evanescent states and (ii) a large density of states (DOS) in the electrodes near the Fermi level. In 2D-material heterostructures, such as CrI_3 magnetic insulators and TMD leads, features of individual layers are, to some extent, preserved due to the weak vdW coupling between them. To characterize these features, we perform first-principles calculations within the density-functional theory (DFT) using the generalized-gradient approximation of the exchange-correlation potential [22], including dispersion forces (vdW-DF-C09) [23–25]. Atomic cores are represented via projector-augmented-wave (PAW) pseudopotentials [26,27] using cutoff energies of 50 Ry and 500 Ry for wave functions and densities, respectively. The Brillouin zone (BZ) is sampled through a $12 \times 12 \times 8$ mesh [28] for bulk electrodes and a $12 \times 12 \times 1$ for heterostructures, employing the QUANTUM ESPRESSO software [29,30].

Here, the effective energy-dependent decay rates in a tunneling barrier are gauged from the complex band structure (CBS) of its bulk form [31,32]. For a magnetic state m, the spin-dependent complex wave vectors ($\kappa_{s,m}$) prominently vary with the in-plane crystal momentum ($\mathbf{k}_\parallel$) and the energy of the evanescent mode. Figure 1(a) illustrates the bulk CrI_3 CBS for both ferromagnetic (FM) and antiferromagnetic (AFM) configurations along the Γ-A, M-L, and K-H symmetry lines of the hexagonal crystal. Despite its larger band gap, the FM spin-minority (red) population have imaginary wave vectors that are comparable to, or at times shorter (e.g., the Γ-A symmetry path near the CrI_3 midgap) than, those of the FM spin-majority (blue) or the AFM cases. This counterintuitive feature tampers with magnetic state differentiation based on spin currents, as discussed below.

Within the Landauer formalism, ballistic conductivity in the magnetic state m is given by $\sigma_m = G_0/A \sum_{s=\uparrow,\downarrow} T_s^m(E)$, where $G_0 = e^2/h \approx 38.7$ μS represents the conductance quantum [33] and A represents the cross-section area of the channel. The quantity $T_s^m(E)$ denotes the transmission probability corresponding to the spin channel s ($s = \uparrow, \downarrow$) [34,35]:

$$T_s^m(E) = \frac{A}{(2\pi)^2} \int dE \int_{2D\,BZ} d^2\mathbf{k}_\parallel \sum_{i,j} t_{i,j}^{s,m}(\mathbf{k}_\parallel, E) \frac{df}{dE}, \quad (1)$$

where $t_{i,j}^{s,m}(\mathbf{k}_\parallel, E)$ and $f(E)$ are the transmission of individual modes and the Fermi distribution, respectively. We first estimate the energy-dependent transmission $\overline{T}_s^m(E)$ solely using CBS of CrI_3 barriers, assuming that all regions of the BZ contribute equally. This ansatz is based on the uniform coverage of the BZ by the Fermi surface of the
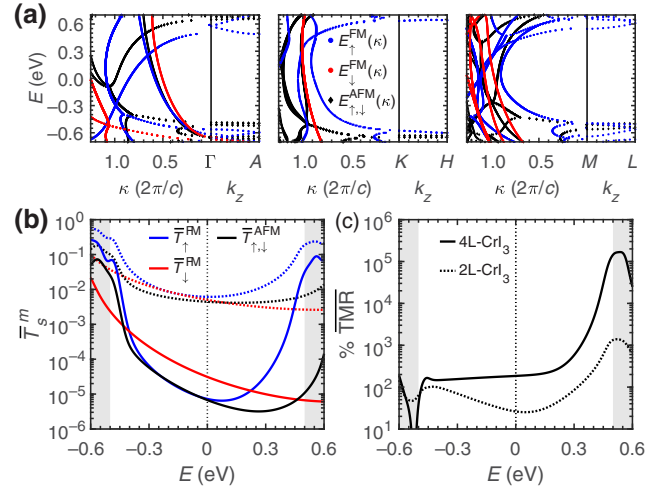

FIG. 1. (a) The CBS for bulk CrI_3 along different symmetry lines (from left to right): Γ-A, K-H, and M-L. The blue (red) lines represent majority (minority) evanescent states produced in the FM configuration, while the gray lines correspond to states in the AFM configuration. (b) Approximate transmission probabilities $\overline{T}_s^m(E)$ and (c) the corresponding $\overline{TMR}$ results obtained from CBS for CrI_3 channels with bilayer (2L) and tetralayer (4L) thicknesses. The energies are referenced to the FM CrI_3 spin-majority midgap and the shaded areas denote the location of the valence and conduction bands.

electrode and is further discussed later. To this end, each mode transmission is computed as

$$\bar{t}_{i,j}^{s,m}(\mathbf{k}_\parallel, E) = \exp[-2\kappa_{s,m}(\mathbf{k}_\parallel, E)\ell], \quad (2)$$

in terms of $\kappa_{s,m}(\mathbf{k}_\parallel, E)$. The tunneling barrier thickness $\ell = Nd$ is expressed in terms of the number of layers N and the interlayer distance ($d \approx 6.4$ Å for CrI_3).

Spin-resolved transmission estimates $\overline{T}_s^m(E)$ for bilayer (2L) and tetralayer (4L) CrI_3 channels in the FM and AFM configurations are obtained using Eqs. (1) and (2). As the channel thickness increases, the transmissions diminish by nearly an order of magnitude per layer for energies within the majority midgap, where longer complex wave vectors reside. As anticipated from the CBS, at these energy levels, spin-majority transmissions in the 4L-CrI_3 FM configuration subside with respect to the spin-minority transmissions, while remaining comparable to transmissions in the AFM configuration (black). Near the band edges, the FM spin-majority transmission decays more slowly and becomes significantly different than those in the AFM configuration.

Differentiation in conductivity between magnetic states is quantified by the TMR:

$$TMR = \frac{|\sigma_{FM} - \sigma_{AFM}|}{\sigma_{min}}, \quad (3)$$

where $\sigma_{min} = \min(\sigma_{AFM}, \sigma_{FM})$ is the least conductive magnetic configuration. In Fig. 1(c), we present the energy-dependent TMR corresponding to 2L- and 4L-thick CrI$_3$ channels using CBS-derived transmissions $\overline{T}_s^m(E)$, aligning the spin-majority valence-band edges (VBEs). Overall, the TMR enhances as the channel thickness increases, albeit with smaller junction conductivities. More importantly, the TMR estimates increase by a few orders of magnitude near the conduction-band edge (CBE) owing to the smaller decay rates of spin-majority carriers at these energy levels (Fig. 1) but shrink drastically near the VBE. Therefore, low-work-function electrodes, injecting carriers near the CBE, may significantly improve the TMR values in these junctions.

To test these predictions, we consider electrode candidates formed by metallic TMD layers [36,37] and compute the work functions ϕ for the most stable polymorphs using DFT [38]. Their work functions range from approximately 4 eV to 7 eV, as illustrated for those with hexagonal lattices (1T and 2H) in Fig. 2(a) and for the remaining (1T' and $Pbca$ space group) phases in the Supplemental Material [38]. Subsequently, we narrow down the TMD candidates by selecting those realized experimentally [39–43], allowing supercells tractable within DFT with small lateral strain ($\lesssim$ 3%) and offering different band alignments with CrI$_3$. Considering these criteria, we focus our efforts on 1T-TaSe$_2$ [44] ($\phi = 4.8$ eV), 2H-NbSe$_2$ [39] ($\phi = 5.6$ eV), and 2H-TaS$_2$ [45] ($\phi = 6.1$ eV) as cases with a low, intermediate, and high work function, respectively.

The Fermi-level DOS of these TMD electrodes is substantially larger than that of graphene [Fig. 2(b)]. Furthermore, we analyze the distribution of states (modes) within the 2D BZ, accounting for the 2×2 epitaxy used in this work when forming interfaces with CrI$_3$. We define the filling factor $\nu(E)$ as the fraction of the bulk electrode 2D BZ that hosts transport modes at a certain energy level (Fig. 2). For the chosen TMD electrodes, nearly ideal Fermi-level filling factors [$\nu(E_F) \sim 1$] are observed, a key assumption in our CBS estimates [Eq. (2)].

Next, we analyze the properties of TMD/CrI$_3$ heterostructures formed with 2L- or 4L-CrI$_3$ channels [38]. To visualize the resulting TMD/2L-CrI$_3$ heterojunction band alignments, in Fig. 3 we compare the spin-resolved projected DOS (PDOS) of neighboring TMD and CrI$_3$. For 1T-TaSe$_2$ (low-work-function) electrodes, the Fermi level falls 0.2 eV below the spin-majority CrI$_3$ CBE; for 2H-NbSe$_2$ and 2H-TaS$_2$ electrodes, the Fermi energies reside 0.4 eV and 0.1 eV above the spin-majority VBE of CrI$_3$, respectively. Owing to enhanced magnetic coupling in these systems, the spin-majority FM CBE is nearly 0.1 eV below the AFM counterpart, while the VBEs remain aligned [35,38].

Spin polarization in the neighboring TMD layer is minor compared to that of the CrI$_3$ channel. Evinced in the
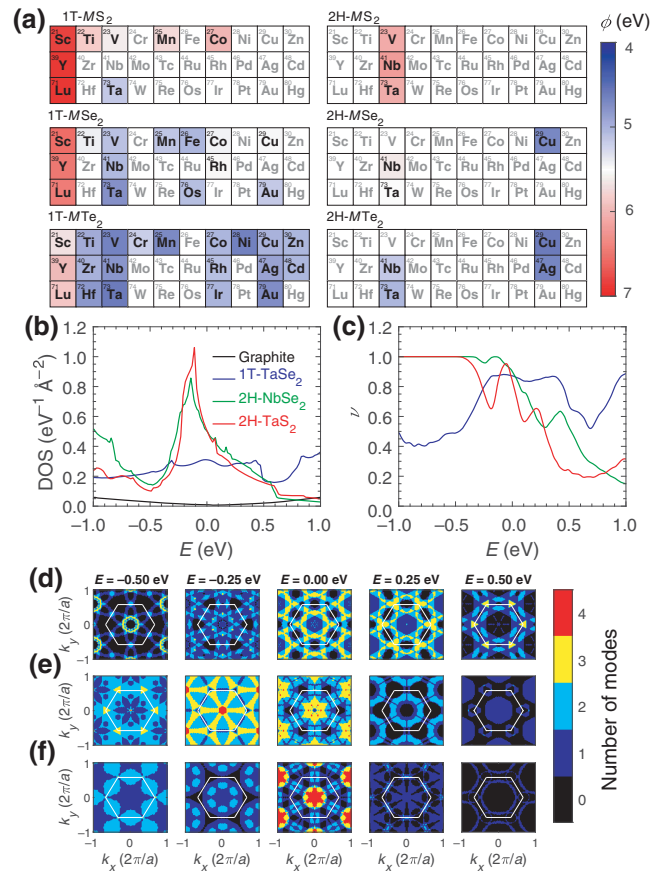

FIG. 2. (a) Color maps of the most stable metallic TMD monolayer work functions, where transition metals are arranged following their location in the periodic table; each row corresponds to a different chalcogen element: S (top), Se (middle), and Te (bottom); the columns denote 1T (left) and 2H (right) phase. (b) The DOS for monolayer TMDs: 1T-TaSe$_2$ (blue), 2H-NbSe$_2$ (green), and 2H-TaS$_2$ (red). For comparison, graphene is also shown. (c) The 2D-BZ filling factor $\nu(E)$ for TMD bulk electrodes with 2×2 epitaxy. (d)–(f) The electron modes of bulk electrodes at various energy levels: (d) 1T-TaSe$_2$, (e) 2H-NbSe$_2$, and (f) 2H-TaS$_2$. Hexagons denote the 2D-BZ edges.

layer-resolved PDOS decomposition, the emergence of metal-induced gap states (MIGS) reveals non-negligible interlayer coupling between the electrode and channel layers in the cases of 1T-TaSe$_2$ and 2H-NbSe$_2$ electrodes. Seen in the insets of Fig. 3, MIGS formed in MTJs with 1T-TaSe$_2$ electrodes extend through the entire band gap, comprised of mainly I p-orbitals followed by Cr d-orbitals. For 2H-NbSe$_2$ electrodes, these states primarily entail I p-orbitals and vanish in the upper half due to the low DOS in the adjacent TMD.

Next, transmissions T_m^s are obtained using the coefficients in Eq. (1) from the NEGF method [46,47], which offers a more accurate (and computationally demanding) characterization of transport. The transmissions for the 2L-
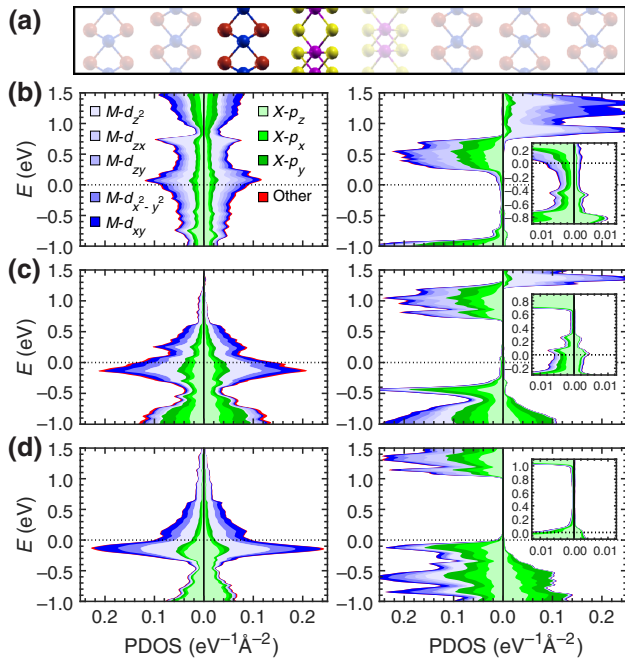
FIG. 3. (a) A schematic of a (2×2)-TMD/(1×1)-CrI$_3$ magnetic tunnel junction, where solid lines mark the supercell of the structure. (b)–(d) Layer-resolved PDOS for the 2L-CrI$_3$ channel and different metal electrodes (from top to bottom): (b) $1T$-TaSe$_2$, (c) $2H$-NbSe$_2$, and (d) $2H$-TaS$_2$. Spin-resolved projections onto localized atomic orbitals on one of the CrI$_3$ layers and its adjacent TMD layer are plotted in the right and left column, respectively.
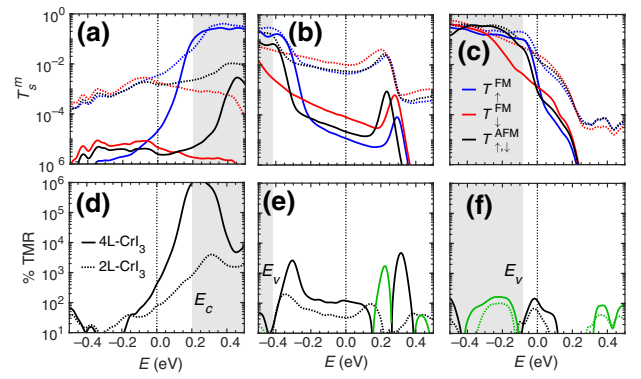

FIG. 4. Transmissions T_s^m (top) and the corresponding TMR (bottom) for 2L- and 4L-thick CrI$_3$ MTJs with different electrodes: (a) $1T$-TaSe$_2$, (b) $2H$-NaSe$_2$, and (c) $2H$-TaS$_2$. For the FM configuration, we plot the spin-majority (blue) and -minority (red) contributions; while for the AFM configuration we average the spin channels (black). The shaded areas denote CrI$_3$ spin-majority band edges. Curves for bilayer (tetralayer) junctions are indicated by dotted (solid) lines. Black (green) portions of the TMR curves denote $\sigma_{\min} = \sigma_{\mathrm{AFM}}$ ($\sigma_{\min} = \sigma_{\mathrm{FM}}$).

and 4L-CrI$_3$ junctions in the FM and AFM configurations using a 36×36 $\mathbf{k}_\parallel$-mesh exhibit most of the features predicted from the CBS (Fig. 4): (i) large transmission values near the band edges; (ii) net transmissions that drop by roughly an order of magnitude per CrI$_3$ layer for carrier energies within the gap; and (iii) for FM cases, current contributions from spin-minority modes that at times surpass those of the spin majority.

Around the Fermi level, heterostructures with $1T$-TaSe$_2$ (low-work-function) electrodes produce spin-majority transmissions in the FM configuration that dominate those of the spin minority or the AFM configuration [Fig. 4(a)], as expected from the CBS (Fig. 1). In contrast, the differences between the FM and AFM spin-majority transmissions [Fig. 4(c)] dwindle with high-work-function leads ($2H$-TaSe$_2$) as the VBEs align [38]. For $2H$-NbSe$_2$ electrodes [Fig. 4(b)], spin transmissions that occur far from band edges are governed by the spin minority and present spikes at energies approximately 0.25 eV above the Fermi level attributed to MIGS (Fig. 3) that effectively shorten the barrier thickness. Accounting for these interactions requires full atomistic descriptions of the interfaces and cannot be anticipated from their bulk properties.

In $1T$-TaSe$_2$/4L-CrI$_3$ junctions, the TMR is twice that of graphite–2L-CrI$_3$ systems at similar conductivity

levels, while conductivities in thinner junctions ($1T$-TaSe$_2$/2L-CrI$_3$) increase by 2 orders of magnitude, with only a small detriment to the TMR [35]. Near the Fermi level, TMR values of approximately 80% and 420% are achieved in 2L- and 4L-CrI$_3$ systems, respectively (Fig. 4). Moreover, in agreement with CBS estimates, these values surge rapidly as the carrier energies approach the CrI$_3$ CBE, a feature that may be accessed via electrostatic gating [8]. Similar results supporting these findings are also obtained for NiTe$_2$/CrBr$_3$ heterostructures [38]. For the $2H$-NbSe$_2$ or $1T$-TaS$_2$ leads, the TMR order of magnitude near the Fermi level is on a par with results in junctions with graphite leads and CBS predictions. However, the TMR results can deviate significantly from those predictions near the midgap and the VBE. These departures emerge due to the reduced filling factor ν for carrier energies moving into the gap [Fig. 2(c)], the presence of MIGS, and the similar FM and AFM decay rates near the VBE.

The applicability of our approach to 2D-material heterostructures stems from the weak interlayer coupling, allowing the properties of the system to be decomposed in terms of their material constituents. An important consideration that ensures successful CBS predictions is a large electrode filling factor $\nu(E)$. CBS estimates face limitations when dominant contributions to transmissions originate from reduced regions of the BZ, due to either strong coherence between layers [48] or their electronic dispersion [49,50]. While the full detailed calculations presented here are limited to those with hexagonal lattices, CBS estimates are expected to be valid in other crystal structures (e.g., $1T'$ and $Pbca$). We thus anticipate that other low-work-function metals—such as $1T$-VTe$_2$

[51], $1T$-NiTe$_2$ [43], $1T'$-MoTe$_2$ [52], $1T'$-WTe$_2$ [53], or $1T'$-ReSe$_2$ [54]—may also yield similar results.

In summary, enhanced conductivities and TMR in 2D-material heterostructures are demonstrated through barrier engineering. We predict TMR improvements using low-work-function TMD electrodes through spin injection near the CrI$_3$ conduction-band edge. Away from the band edges, where modes decay more rapidly, results are susceptible to lead-channel interactions. Additionally, these systems offer up to 3-orders-of-magnitude-greater conductivities than those with graphitic electrodes. The approach employed here enables the data-driven design of 2D-material heterostructures and agrees with the NEGF results. The method is based on first-principles calculations of bulk electrodes and channels, circumventing computationally challenging descriptions of full heterostructures. By identifying candidate materials based on their bulk properties, our methodology may accelerate the guided design of devices based on 2D materials.

[1] A. K. Geim and I. V. Grigorieva, Van der Waals heterostructures, Nature **499**, 419 (2013).

[2] Y. Liu, S. Zhang, J. He, Z. M. Wang, and Z. Liu, Recent progress in the fabrication, properties, and devices of heterostructures based on 2D materials, Nano-Micro Lett. **11**, 13 (2019).

[3] D. R. Klein, D. MacNeill, J. L. Lado, D. Soriano, E. Navarro-Moratalla, K. Watanabe, T. Taniguchi, S. Manni, P. Canfield, J. Fernandez-Rossier, *et al.*, Probing magnetism in 2D van der Waals crystalline insulators via electron tunneling, Science **360**, 1218 (2018).

[4] H. H. Kim, B. Yang, S. Tian, C. Li, G.-X. Miao, H. Lei, and A. W. Tsen, Tailored tunnel magnetoresistance response in three ultrathin chromium trihalides, Nano Lett. **19**, 5739 (2019).

[5] T. Song, X. Cai, M. W.-Y. Tu, X. Zhang, B. Huang, N. P. Wilson, K. L. Seyler, L. Zhu, T. Taniguchi, K. Watanabe, *et al.*, Giant tunneling magnetoresistance in spin-filter van der Waals heterostructures, Science **360**, 1214 (2018).

[6] Z. Wang, I. Gutiérrez-Lezama, N. Ubrig, M. Kroner, M. Gibertini, T. Taniguchi, K. Watanabe, A. Imamoğlu, E. Giannini, and A. F. Morpurgo, Very large tunneling magnetoresistance in layered magnetic semiconductor CrI$_3$, Nat. Commun. **9**, 1 (2018).

[7] H. H. Kim, B. Yang, T. Patel, F. Sfigakis, C. Li, S. Tian, H. Lei, and A. W. Tsen, One million percent tunnel magnetoresistance in a magnetic van der Waals heterostructure, Nano Lett. **18**, 4885 (2018).

[8] T. Song, M. W.-Y. Tu, C. Carnahan, X. Cai, T. Taniguchi, K. Watanabe, M. A. McGuire, D. H. Cobden, D. Xiao, W. Yao, *et al.*, Voltage control of a van der Waals spin-filter magnetic tunnel junction, Nano Lett. **19**, 915 (2019).

[9] A. Manchon, J. Železný, I. M. Miron, T. Jungwirth, J. Sinova, A. Thiaville, K. Garello, and P. Gambardella, Current-induced spin-orbit torques in ferromagnetic and antiferromagnetic systems, Rev. Mod. Phys. **91**, 035004 (2019).

[10] K. Dolui, M. D. Petrović, K. Zollner, P. Plecháč, J. Fabian, and B. K. Nikolić, Proximity spin-orbit torque on a two-dimensional magnet within van der Waals heterostructure: Current-driven antiferromagnet-to-ferromagnet reversible nonequilibrium phase transition in bilayer CrI$_3$, Nano Lett. **20**, 2288 (2020).

[11] L. Zhang, J. Zhou, H. Li, L. Shen, and Y. P. Feng, Recent progress and challenges in magnetic tunnel junctions with 2D materials for spintronic applications, Appl. Phys. Rev. **8**, 021308 (2021).

[12] T. R. Paudel and E. Y. Tsymbal, Spin filtering in CrI$_3$ tunnel junctions, ACS Appl. Mater. Interfaces **11**, 15781 (2019).

[13] J. Zhou, J. Qiao, C.-G. Duan, A. Bournel, K. L. Wang, and W. Zhao, Large tunneling magnetoresistance in VSe$_2$/MoS$_2$ magnetic tunnel junction, ACS Appl. Mater. Interfaces **11**, 17647 (2019).

[14] L. V. Begunovich, A. V. Kuklin, M. A. Visotin, A. A. Kuzubov, F. N. Tomilin, A. S. Tarasov, Y. G. Mikhalev, and P. V. Avramov, Triple VTe$_2$/graphene/VTe$_2$ heterostructures as perspective magnetic tunnel junctions, Appl. Surf. Sci. **510**, 145315 (2020).

[15] F. Li, B. Yang, Y. Zhu, X. Han, and Y. Yan, Four distinct resistive states in van der Waals full magnetic $1T$-VSe$_2$/CrI$_3$/$1T$-VSe$_2$ tunnel junction, Appl. Surf. Sci. **505**, 144648 (2020).

[16] M. Arai, R. Moriya, N. Yabuki, S. Masubuchi, K. Ueno, and T. Machida, Construction of van der Waals magnetic tunnel junction using ferromagnetic layered dichalcogenide, Appl. Phys. Lett. **107**, 103107 (2015).

[17] W. Wang, A. Narayan, L. Tang, K. Dolui, Y. Liu, X. Yuan, Y. Jin, Y. Wu, I. Rungger, S. Sanvito, *et al.*, Spin-valve effect in NiFe/MoS$_2$/NiFe junctions, Nano Lett. **15**, 5261 (2015).

[18] K. Zhao, Y. Xing, J. Han, J. Feng, W. Shi, B. Zhang, and Z. Zeng, Magnetic transport property of NiFe/WSe$_2$/NiFe spin valve structure, J. Magn. Magn. Mater. **432**, 10 (2017).

[19] M. F. Khan, H. Kim, G. Nazir, S. Jung, and J. Eom, Layer dependent magnetoresistance of vertical MoS$_2$ magnetic tunnel junctions, Nanoscale **10**, 16703 (2018).

[20] Xinlu Li, Jing-Tao Lü, Jia Zhang, Long You, Yurong Su, and Evgeny Y. Tsymbal, Spin-dependent transport in van der Waals magnetic tunnel junctions with Fe$_3$GeTe$_2$ electrodes, Nano Lett. **19**, 5133 (2019).

[21] P. Kumar, A. Kumar, and D. Kaur, Spin valve effect in sputtered FL-MoS$_2$ and ferromagnetic shape memory alloy based magnetic tunnel junction, Ceram. Int. **47**, 4587 (2021).

[22] J. P. Perdew, K. Burke, and M. Ernzerhof, Generalized Gradient Approximation Made Simple, Phys. Rev. Lett. **78**, 1396 (1997).

[23] M. Dion, H. Rydberg, E. Schröder, D. C. Langreth, and B. I. Lundqvist, Van der Waals Density Functional for General Geometries, Phys. Rev. Lett. **92**, 246401 (2004).

[24] T. Thonhauser, V. R. Cooper, S. Li, A. Puzder, P. Hyldgaard, and D. C. Langreth, Van der Waals density functional: Self-consistent potential and the nature of the van der Waals bond, Phys. Rev. B **76**, 125112 (2007).

[25] V. R. Cooper, Van der Waals density functional: An appropriate exchange functional, Phys. Rev. B **81**, 161104 (2010).

[26] P. E. Blöchl, Projector augmented-wave method, Phys. Rev. B **50**, 17953 (1994).

[27] A. D. Corso, Pseudopotentials periodic table: From H to Pu, Comput. Mater. Sci. **95**, 337 (2014).

[28] H. J. Monkhorst and J. D. Pack, Special points for Brillouin-zone integrations, Phys. Rev. B **13**, 5188 (1976).

[29] P. Giannozzi *et al.*, Advanced capabilities for materials modelling with QUANTUM ESPRESSO, J. Phys.: Condens. Matter **29**, 465901 (2017).

[30] A. Smogunov, A. D. Corso, and E. Tosatti, Ballistic conductance of magnetic Co and Ni nanowires with ultrasoft pseudopotentials, Phys. Rev. B **70**, 045417 (2004).

[31] M. G. Reuter, A unified perspective of complex band structure: Interpretations, formulations, and applications, J. Phys.: Condens. Matter **29**, 053001 (2016).

[32] A. M. Pfeifle and M. A. Kuroda, Tunable contact resistance in transition metal dichalcogenide lateral heterojunctions, Phys. Rev. Mater. **4**, 024002 (2020).

[33] S. Datta, *Electronic Transport in Mesoscopic Systems, Cambridge Studies in Semiconductor Physics and Microelectronic Engineering* (Cambridge University Press, Cambridge, 1995).

[34] A. D. Carlo, P. Vogl, and W. Pötz, Theory of Zener tunneling and Wannier-Stark states in semiconductors, Phys. Rev. B **50**, 8358 (1994).

[35] J. J. Heath, M. Costa, M. Buongiorno-Nardelli, and M. A. Kuroda, Role of quantum confinement and interlayer coupling in CrI_3-graphene magnetic tunnel junctions, Phys. Rev. B **101**, 195439 (2020).

[36] Q. H. Wang, K. Kalantar-Zadeh, A. Kis, J. N. Coleman, and M. S. Strano, Electronics and optoelectronics of two-dimensional transition metal dichalcogenides, Nat. Nanotechnol. **7**, 699 (2012).

[37] S. Curtarolo, W. Setyawan, G. L. W. Hart, M. Jahnatek, R. V. Chepulskii, R. H. Taylor, S. Wang, J. Xue, K. Yang, O. Levy, *et al.*, AFLOW: An automatic framework for high-throughput materials discovery, Comput. Mater. Sci. **58**, 218 (2012).

[38] See the Supplemental Material at http://link.aps.org/supplemental/10.1103/PhysRevApplied.16.L041001 for TMD electrode prioritization, geometric properties of TMD/CrX_3 structures, and $NiTe_2$/$CrBr_3$ performance.

[39] M Marezio, P. D. Dernier, A Menth, and G. W. Hull Jr, The crystal structure of $NbSe_2$ at 15 K, J. Solid State Chem. **4**, 425 (1972).

[40] D. E. Moncton, J. D. Axe, and F. J. DiSalvo, Neutron scattering study of the charge-density wave transitions in $2H$-$TaSe_2$ and $2H$-$NbSe_2$, Phys. Rev. B **16**, 801 (1977).

[41] G. A. Wiegers, J. L. de Boer, A. Meetsma, and S. van Smaalen, Domain structure and refinement of the triclinic superstructure of $1T$-$TaSe_2$ by single crystal x-ray diffraction, Zeitschrift für Kristallographie-Cryst. Mater. **216**, 45 (2001).

[42] A Meetsma, G. A. Wiegers, R. J. Haange, and J. L. de Boer, Structure of $2H$-TaS_2, Acta Crystallogr. Sect. C: Cryst. Struct. Commun. **46**, 1598 (1990).

[43] C. Xu, B. Li, W. Jiao, W. Zhou, B. Qian, R. Sankar, N. D. Zhigadlo, Y. Qi, D. Qian, F.-C. Chou, *et al.*, Topological type-II Dirac fermions approaching the Fermi level in a transition metal dichalcogenide $NiTe_2$, Chem. Mater. **30**, 4823 (2018).

[44] F. J. Di Salvo, R. G. Maines, J. V. Waszczak, and R. E. Schwall, Preparation and properties of $1T$-$TaSe_2$, Solid State Commun. **14**, 497 (1974).

[45] F. R. Gamble, J. H. Osiecki, and F. J. DiSalvo, Some superconducting intercalation complexes of TaS_2 and substituted pyridines, J. Chem. Phys. **55**, 3525 (1971).

[46] M. B. Nardelli, Electronic transport in extended systems: Application to carbon nanotubes, Phys. Rev. B **60**, 7828 (1999).

[47] M. B. Nardelli, F. T. Cerasoli, M. Costa, S. Curtarolo, R. De Gennaro, M. Fornari, L. Liyanage, A. R. Supka, and H. Wang, PAOFLOW: A utility to construct and operate on *ab initio* Hamiltonians from the projections of electronic wavefunctions on atomic orbital bases, including characterization of topological materials, Comput. Mater. Sci. **143**, 462 (2018).

[48] W. H. Butler, X.-G. Zhang, T. C. Schulthess, and J. M. MacLaren, Spin-dependent tunneling conductance of Fe|MgO|Fe sandwiches, Phys. Rev. B **63**, 054416 (2001).

[49] V. M. Karpan, G. Giovannetti, P. A. Khomyakov, M. Talanana, A. A. Starikov, M. Zwierzycki, J. van den Brink, G. Brocks, and P. J. Kelly, Graphite and Graphene as Perfect Spin Filters, Phys. Rev. Lett. **99**, 176602 (2007).

[50] M. A. Kuroda, J. Tersoff, D. M. Newns, and G. J. Martyna, Conductance through multilayer graphene films, Nano Lett. **11**, 3629 (2011).

[51] X. Ma, T. Dai, S. Dang, S. Kang, X. Chen, W. Zhou, G. Wang, H. Li, P. Hu, Z. He, *et al.*, Charge density wave phase transitions in large-scale few-layer $1T$-VTe_2 grown by molecular beam epitaxy, ACS Appl. Mater. Interfaces **11**, 10729 (2019).

[52] C. H. Naylor, W. M. Parkin, J. Ping, Z. Gao, Y. R. Zhou, Y. Kim, F. Streller, R.W. Carpick, A.M. Rappe, M. Drndić, *et al.*, Monolayer single-crystal $1T'$-$MoTe_2$ grown by chemical vapor deposition exhibits weak antilocalization effect, Nano Lett. **16**, 4297 (2016).

[53] M. J. Mleczko, R. L. Xu, K. Okabe, H.-H. Kuo, I. R. Fisher, H.-S. P. Wong, Y. Nishi, and E. Pop, High current density and low thermal conductivity of atomically thin semimetallic WTe_2, ACS Nano **10**, 7507 (2016).

[54] A. Apte, A. Krishnamoorthy, J. A. Hachtel, S. Susarla, J. Yoon, L. M. Sassi, P. Bharadwaj, J. M. Tour, J. C. Idrobo, R. K. Kalia, *et al.*, Two-dimensional lateral epitaxy of $2H$($MoSe_2$)-$1T'$($ReSe_2$) phases, Nano Lett. **19**, 6338 (2019).